

Manuscript version: Author's Accepted Manuscript

The version presented in WRAP is the author's accepted manuscript and may differ from the published version or Version of Record.

Persistent WRAP URL:

<http://wrap.warwick.ac.uk/167201>

How to cite:

Please refer to published version for the most recent bibliographic citation information. If a published version is known of, the repository item page linked to above, will contain details on accessing it.

Copyright and reuse:

The Warwick Research Archive Portal (WRAP) makes this work by researchers of the University of Warwick available open access under the following conditions.

Copyright © and all moral rights to the version of the paper presented here belong to the individual author(s) and/or other copyright owners. To the extent reasonable and practicable the material made available in WRAP has been checked for eligibility before being made available.

Copies of full items can be used for personal research or study, educational, or not-for-profit purposes without prior permission or charge. Provided that the authors, title and full bibliographic details are credited, a hyperlink and/or URL is given for the original metadata page and the content is not changed in any way.

Publisher's statement:

Please refer to the repository item page, publisher's statement section, for further information.

For more information, please contact the WRAP Team at: wrap@warwick.ac.uk.

1 Probing Viscosity and Structural Variations in $\text{CaF}_2\text{-SiO}_2\text{-MnO}$ Welding Fluxes

2 Yanyun Zhang^{1,2}, Zhanjun Wang^{1,2,3}, Jiawen Zhang^{1,2}, Zushu Li⁴, Somnath Basu⁵, and Cong
3 Wang^{1,2*}

4 ¹ Key Laboratory for Ecological Metallurgy of Multimetallic Mineral (Ministry of Education),
5 Northeastern University, Shenyang 110819, China

6 ² School of Metallurgy, Northeastern University, Shenyang 110819, China

7 ³ State Key Laboratory of Advanced Welding and Joining, Harbin Institute of Technology, Harbin
8 150001, China

9 ⁴ WMG, University of Warwick, Coventry, CV4 7AL, United Kingdom

10 ⁵ Department of Metallurgical Engineering and Materials Science, Indian Institute of Technology,
11 Bombay, 400076, India

12 * Corresponding author. Prof., Ph.D.; Tel.: +86 15702435155; Fax: +86 24 23906316

13 E-mail address: wangc@smm.neu.edu.cn (C. Wang)

14 ABSTRACT

15 Recent demand on welding fluxes for high-strength low-alloy steel grades has necessitated the
16 development of CaF_2 -free fluxes towards high heat input applications. To meet such requirements, a
17 flux design strategy has been postulated by varying $\text{MnO}/(\text{CaF}_2+\text{MnO})$ mass ratio in the $\text{CaF}_2\text{-SiO}_2\text{-}$
18 MnO flux system. The effect of MnO substitution for CaF_2 on the flux viscosity and structure has
19 been investigated, and a quantitative relationship between viscosity and structural units has been put
20 forward. In addition, it has been suggested that the degree of polymerization (DOP) of silicate
21 network is reduced with increasing $\text{MnO}/(\text{CaF}_2+\text{MnO})$ mass ratio, indicating MnO plays the role of
22 network-breaker. The spectra of F_{1s} and ^{19}F prove that F^- predominantly bonds with Ca^{2+} rather than
23 Si^{4+} , revealing CaF_2 acts as a diluent and does not effectively depolymerize the silicate network.
24 Linear correlations can be obtained between the logarithm viscosity and the average non-bridging

oxygen per silicon atom (NBO/Si), which can potentially be used as a DOP index to quantify the impact of silicate structure on the viscosity of the flux.

KEYWORDS: Welding flux; Structure; Viscosity; MnO; CaF₂

I. INTRODUCTION

High heat input submerged arc welding (SAW) has been widely used for welding thick steel plate products due to its high efficiency and low-cost.^[1, 2] However, high heat input may cause deteriorated mechanical properties of the welded products as a result of coarsened grains.^[3] Recent studies have demonstrated that welding fluxes play vital roles in such as improving alloying element transfer, stabilizing the arc, and refining the weld pool, and could be utilized as a countermeasure to offset adverse impact caused by high heat input welding.^[4-6]

Physicochemical properties of the welding fluxes, including viscosity, softening temperature, and crystallization behaviors are essential indicators for flux design.^[4, 7] In particular, flux viscosity directly affects weld formability, slag-metal reaction kinetics, alloying element transfer behaviors, and slag detachability.^[5, 8] It is widely acknowledged that flux viscosity is inherently rooted in the structures of the fluxes.^[9-11] Thus, it is essential to determine the flux viscosity and structural characteristics quantitatively for designing fluxes with targeted properties.

CaF₂-SiO₂-MnO fused fluxes, owing to their satisfactory chemical homogeneity, fine anti-porosity property, and excellent thermal crack resistance, have been employed for SAW construction of high-strength low-alloy (HSLA) steel grades.^[7] CaF₂ serves as a diluent to reduce the melting temperature and viscosity during welding.^[12] However, it is a growing recognition that the CaF₂ content shall be limited as it may pose environmental and ergonomic threats. To achieve the desired

low-fluoride fluxes, one major challenge is to elucidate the mechanism of CaF_2 in altering physicochemical properties of pertinent fluxes. Nevertheless, studies undertaken so far provide contradictory evidence concerning the roles of CaF_2 in flux/slag structure.^[13-17] The addition of CaF_2 to silicate glasses is reported to lead to the depolymerization of silicate networks owing to the abundant presence of Si-F bonds,^[13, 14] while CaF_2 is also found to act as a diluent and not contribute to the breakage of Si-O-Si bonds.^[15, 16] On the other hand, it has been proven that MnO acts as a network modifier and reduces fluxes viscosity,^[11, 18] so that it can be used to replace CaF_2 . Moreover, MnO and SiO_2 are invariably decomposed into Mn, Si, and O under arc plasma, promoting Mn, Si, O transfer from fluxes to weld metals.^[7, 19, 20] Mn-containing and Si-containing inclusions could promote the nucleation of acicular ferrites with interlocking structures, which could delay crack propagation in the welded products.^[21, 22] However, detailed studies on the effect of MnO on viscosity remain limited for fluxes with relatively low MnO contents (< 10 mass pct).^[11, 18, 23]

In the present study, a flux design strategy by replacing CaF_2 with MnO has been postulated. The effect of MnO substitution for CaF_2 on viscosity and structures of CaF_2 - SiO_2 -MnO fluxes at high temperatures has been thoroughly investigated by means of Raman spectra, X-ray photoelectron spectroscopy (XPS), and magic angular spinning nuclear magnetic resonance (MAS-NMR). Moreover, the structural roles of MnO and CaF_2 in CaF_2 - SiO_2 -MnO fluxes were elucidated. The relationship between the viscosity and structure of the CaF_2 - SiO_2 -MnO fluxes has been quantitatively established. This study aims to offer refreshed understanding with regard to the development of fluorine-free welding fluxes.

II. EXPERIMENTAL PROCEDURE AND METHODS

A. Fluxes Preparation

Fluxes were prepared from reagent-grade chemicals of CaF_2 (> 98.5 mass pct), SiO_2 (> 99.7 mass pct), and MnO (>99.0 mass pct). Chemical compositions of the fluxes with different $\text{MnO}/(\text{MnO}+\text{CaF}_2)$ mass ratios are shown in Table I, in which the flux numbers represent corresponding nominal MnO mass percentages. Totally 200 g reagents were fully mixed in a three-dimensional mixing machine for 0.5 hours, then pressed to 4 cylinders ($\Phi 50 \text{ mm} \times H 20 \text{ mm}$) at 20 MPa pressure. The cylinders were placed in a molybdenum crucible ($\Phi 60 \text{ mm} \times H 120 \text{ mm}$) and melted in a vertical tube furnace. The furnace temperature was raised to 1823 K and held for 1 hour to ensure complete homogenization of flux under high purity Ar gas (99.999 vol pct). The premelted fluxes were quenched in cold water (273 K), dried, and grounded into powders (< 74 μm) for viscosity measurements and structural analysis.

Table I Chemical compositions of synthetic fluxes (mass pct).

Fluxes No.		CaF_2	SiO_2	MnO	$\text{MnO}/(\text{CaF}_2+\text{MnO})$
F10	Designed	50.00	40.00	10.00	0.17
	After-quench	49.05(± 1.30)	40.85(± 0.23)	10.10(± 0.20)	0.17
F20	Designed	40.00	40.00	20.00	0.33
	After-quench	39.25(± 1.26)	40.76(± 0.24)	20.19(± 0.22)	0.34
F30	Designed	30.00	40.00	30.00	0.50
	After-quench	29.16(± 1.28)	40.63(± 0.25)	30.21(± 0.26)	0.51
F40	Designed	20.00	40.00	40.00	0.67
	After-quench	19.02(± 1.25)	40.53(± 0.23)	40.45(± 0.23)	0.68
F50	Designed	10.00	40.00	50.00	0.83
	After-quench	9.29(± 1.21)	40.21(± 0.21)	50.50(± 0.25)	0.84

Chemical compositions of the after-quench fluxes were characterized using X-ray fluorescence (XRF, ZSX Primus IV, Rigaku, Japan), as listed in Table I, which shows negligible differences as compared to nominal compositions. The crystalline states of the fluxes were characterized by X-ray powder diffraction (XRD, D8 Advance, Bruker, Germany), and corresponding XRD patterns over the range of 10-90° were recorded by a Cu $K\alpha$ radiation ($\lambda=0.154 \text{ nm}$) at a scan rate of 4 °/min.

84 B. *Viscosity Measurement*

85 Viscosity measurements were performed by using a melt physical property comprehensive
86 testing instrument (VDR-16000, Chongqing University, China) with a Brookfield digital viscometer
87 (model DV2T, Brookfield Engineering Laboratories, USA). The accuracy and the repeatability of the
88 viscometer according to the machine manufacturer were ± 1.0 pct and ± 0.2 pct, respectively. The
89 viscometer was calibrated by the standard silicone oils (0.5 Pa·s) at 298 K. High purity Ar flow (0.5
90 L/min) was injected from the bottom of the alumina tube to protect the Mo crucible and shaft from
91 oxidation. The molybdenum crucible ($\Phi 50 \times H 100$ mm) containing 150 g of the quenched fluxes was
92 positioned in the uniform temperature zone of the tube furnace, which was calibrated by a reference
93 B-type thermocouple and controlled within ± 2 K using a proportional integral derivative controller.
94 The furnace was heated to 1773 K and maintained for 30 minutes to ensure the flux homogeneity.
95 Afterwards, a molybdenum spindle was slowly sunk into the liquid fluxes and kept at a distance of 20
96 mm above the crucible bottom. The flux viscosity in the temperature range of 1300 to 1773 K was
97 measured at the interval of 20 K after holding the sample at the measuring temperatures for 20
98 minutes to ensure thermal equilibrium. The final viscosity values at the target temperature were the
99 average results obtained at three rotation speeds (50, 75, and 100 r/min) and the deviation of all
100 measured experimental data from the average value is less than 3 pct.

101 C. *Spectral Measurements*

102 Structural analysis of the fluxes was performed using Raman spectra, XPS, and MAS-NMR
103 techniques. Raman spectra measurements were conducted using a laser confocal Raman spectrometer
104 (HR800, Horiba, France) with an excitation wavelength of 488 nm. The range of the measured

frequency band was from 400 to 1600 cm^{-1} , and the spectra resolution was in the order of 1 cm^{-1} . XPS (EscaLab 250Xi, Thermo Fischer, USA) was employed to measure O_{1s} and F_{1s} binding energy of the quenched fluxes. The XPS results were calibrated using C_{1s} binding energy at 284.8 eV. Detailed fitting results of Raman and XPS spectra were provided in Appendix A. Solid-state ^{19}F NMR measurements were recorded using a 400 MHz MAS-NMR (Avance III 400M, Bruker, Germany) spectrometer at a resonance frequency of 376.7 MHz with a spinning rate of 8 kHz. The MAS-NMR spectra of ^{19}F referenced to CaF_2 taken at -108 ppm,^[24] and baseline correction was processed using MestreNova 12.0.0 software.

III. RESULTS AND DISCUSSIONS

A. Effect of $\text{MnO}/(\text{MnO}+\text{CaF}_2)$ Mass Ratio on Flux Viscosity

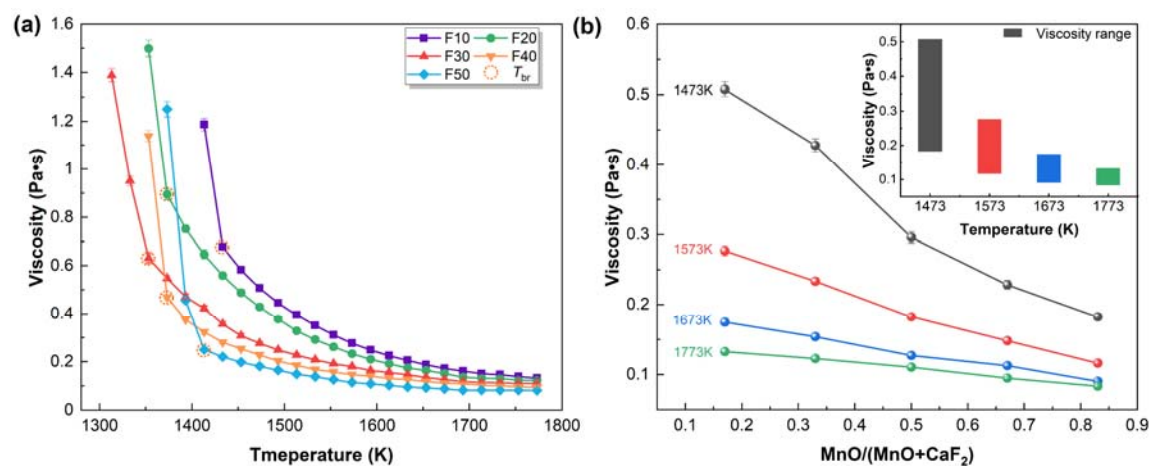


Figure 1—Flux viscosity as a function of (a) temperature, and (b) $\text{MnO}/(\text{MnO}+\text{CaF}_2)$ mass ratio.

Inset figure shows the viscosity range of flux with increasing $\text{MnO}/(\text{MnO}+\text{CaF}_2)$ mass ratio from 0.17 to 0.84 at given temperatures.

Viscosity values of all the five fluxes measured at various temperatures are shown in Figure 1(a).

It can be observed that the viscosity increases smoothly with decreasing temperature until it reaches

the break temperature (T_{br}), which is a significant parameter indicating the precipitation of crystalline phases in sizeable quantities and is generally employed to distinguish fully liquid region ($>T_{br}$) and solid/liquid coexisting region ($<T_{br}$) in molten flux.^[25-27] As shown in Figure 1(a), corresponding T_{br} values for fluxes from F10 through F50 are 1433, 1373, 1353, 1373, 1413 K, respectively. T_{br} values are obviously lower than the melting point of the weld metal, which could avoid pit formation on the surface of the weld metal during solidification.^[12] Figure 1(b) shows the effect of MnO/(MnO+CaF₂) mass ratio on the viscosity at varied temperatures. As shown in Figure 1(b), at any given temperature, viscosity continuously decreases with the substitution of CaF₂ by MnO. At 1473K, flux viscosity substantially decreases from 0.51 to 0.18 Pa·s with increasing MnO/(MnO+CaF₂) mass ratio from 0.17 to 0.84. However, flux viscosity only slightly decreases from 0.13 to 0.08 Pa·s at 1773K. Thus, the effect of the MnO/(MnO+CaF₂) mass ratio is more dominant at lower temperatures (1473 and 1573 K), as shown in the inset figure of Figure 1(b), which is consistent with the trend reported by previous researchers.^[28, 29] It is noted that viscosity values of all fluxes at 1673 K are ranging from 0.09 to 0.17 Pa·s, indicating excellent fluidity and mass transfer properties, which also fall nicely within the requirements for SAW conditions.^[12] Therefore, it is possible to design CaF₂-free fluxes with suitable viscosity for SAW applications.

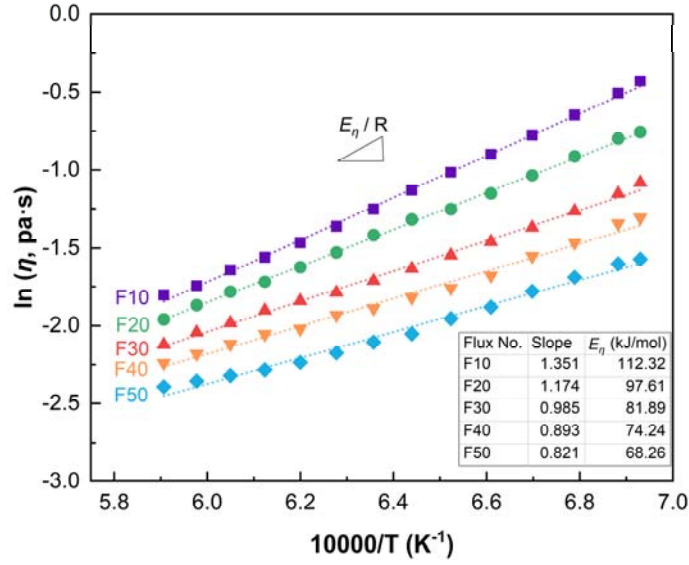


Figure 2—Arrhenius plot for the fluxes in fully liquid regions.

To understand the mechanism of viscosity variations, the Arrhenius equation (Equation [1]) is employed to derive the relationship between viscosity and temperature.^[30]

$$\ln \eta = \ln A_\eta + \frac{E_\eta}{R} \times \frac{1}{T} \quad [1]$$

where η (Pa·s), A_η , E_η (J/mol), R ([J/(mol·K)]), and T (K) denote viscosity, pre-exponential factor, activation energy for the viscous flow, universal gas constant, and absolute temperature, respectively.

In associated liquids featuring network structures, E_η means the energy barrier that cohesive flow units in slags have to overcome,^[31] and the value of E_η is expected to be constant for a fully liquid flux.^[32] Accordingly, $\ln \eta$ values have been plotted against reciprocal temperatures in Figure 2, which

shows a linear relationship for the targeted fluxes in fully liquid regions, indicating viscosity variation is dictated by thermal activation energy. Furthermore, it is found that E_η values decrease from 112.32 to 68.26 kJ/mol with increasing MnO/(MnO+CaF₂) mass ratio from 0.17 to 0.84, indicating the reduction of liquid shearing resistance for viscous flow. From the ionic interaction of view,^[33, 34]

decreasing E_η is enabled by the flow unit change in the order of Si-O-Si and Si-O-Mn. In addition,

relaxation effect of cationic species induced by the formation of Si-O-Mn could reduce E_η of the viscous flow.^[35, 36]

B. *Effect of MnO/(MnO+CaF₂) Mass Ratio on Flux Structure*

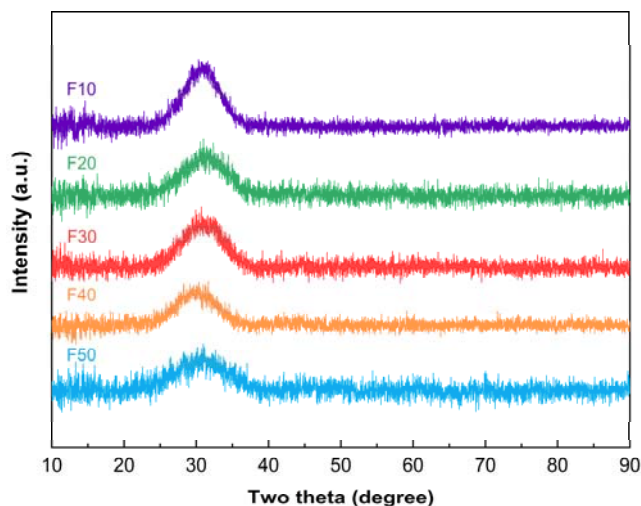


Figure 3—XRD patterns of the quenched fluxes.

Figure 3 shows XRD patterns of the fluxes with different MnO/(MnO+CaF₂) mass ratios quenched from 1823 K. It can be observed that all patterns unanimously show broad diffusive peaks in the 2θ range of 20 to 40 deg, confirming the amorphous state of the quenched fluxes. Homogeneous amorphous fluxes are considered to preserve the molten structure details, which could be used for analyzing the fluxes structures at high temperatures.^[31, 37] In addition, amorphous fluxes are potentially beneficial for weldability as it could improve weld formability, slag detachability, and arc stability in SAW process.^[38, 39]

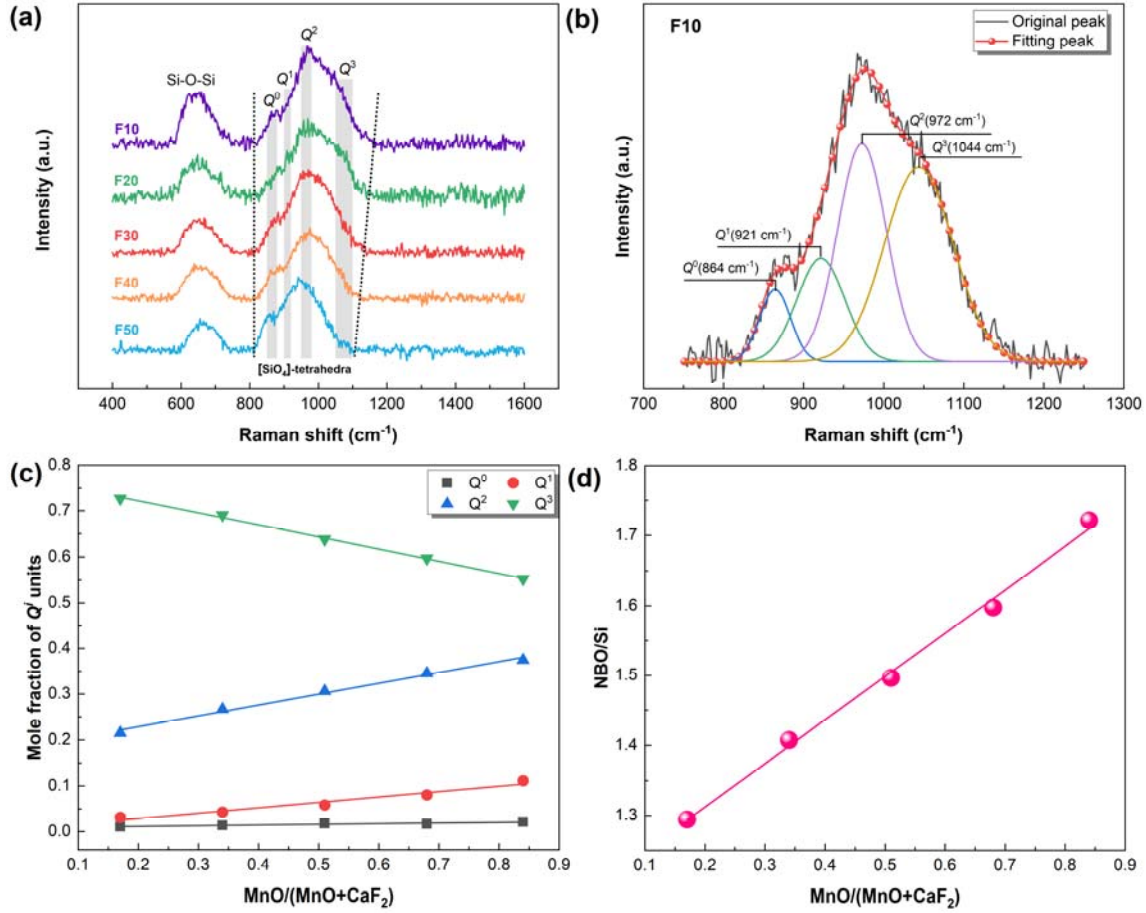


Figure 4 —(a) Raman spectra of the fluxes, (b) typical Raman deconvolution results of F10, (c) mole fraction of different [SiO₄]-tetrahedra units as a function of MnO/(MnO+CaF₂) mass ratio, and (d) degree of polymerization as a function of MnO/(MnO+CaF₂) mass ratio.

Raman spectra of the fluxes tested as a function of Raman shift ranging from 400 to 1600 cm⁻¹ are plotted in Figure 4(a). As can be seen, all spectra exhibit two bands: a higher frequency band (800-1160 cm⁻¹) and a lower frequency band (590-760 cm⁻¹). The lower frequency band is usually ascribed to symmetric stretching vibration of Si-O-Si, which shows no apparent shift with MnO substitution for CaF₂. The higher frequency band is related to the symmetric stretching vibration bands of Si-O in [SiO₄]-tetrahedra units.^[10] In the frequency region of [SiO₄]-tetrahedra units, five types of [SiO₄]-tetrahedra units are defined as Q^i (i is the number of bridging oxygen in a [SiO₄]-

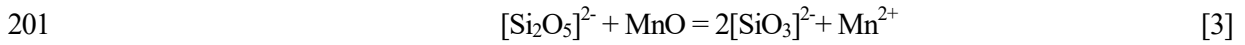
tetrahedra unit, and i ranges from 0 to 4), wherein five types of $[\text{SiO}_4]$ -tetrahedra units are Q^0 ($[\text{SiO}_4]^{4-}$, monomer), Q^1 ($[\text{Si}_2\text{O}_7]^{6-}$, dimer), Q^2 ($[\text{Si}_2\text{O}_6]^{4-}$, chain), Q^3 ($[\text{Si}_4\text{O}_{11}]^{6-}$, sheet), and Q^4 (SiO_2 , fully polymerized),^[10, 30] respectively. As marked in Figure 4(a), Q^0 to Q^3 bands are located at ranges of 850-880, 900-920, 950-980, 1050-1100 cm^{-1} , respectively. The band of $[\text{SiO}_4]$ -tetrahedra (800-1160 cm^{-1}) moves to a lower frequency range (800-1100 cm^{-1}) with the increasing mass ratio of $\text{MnO}/(\text{MnO}+\text{CaF}_2)$ from 0.17 to 0.84, indicating that silicate networks are gradually depolymerized with CaF_2 being substituted by MnO .

Various $[\text{SiO}_4]$ -tetrahedra units overlap within higher frequency bands. Raman spectra have been deconvoluted by the Gaussian fitting model.^[31, 40] Figure 4(b) shows typical Raman deconvolution results of F10 (The rest of the deconvolution results are provided in Figure A1). According to the areas of the obtained peaks (A_i) and the Raman scattering coefficient (S_i) of Q^i , mole fractions (X_i) of various Q^i could be calculated by Equation [2],^[41] and the values of S_0 , S_1 , S_2 , and S_3 are 1, 0.514, 0.242, and 0.09,^[40, 41] respectively.

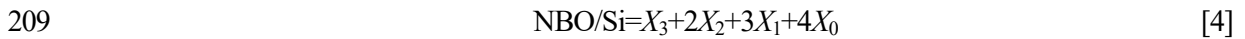
$$X_i = \frac{A_i}{S_i} / \left(\sum_{i=0}^3 \frac{A_i}{S_i} \right) \quad [2]$$

Mole fractions of Q^i as a function of $\text{MnO}/(\text{MnO}+\text{CaF}_2)$ mass ratios are plotted in Figure 4(c). As observed, mole fractions of Q^2 and Q^1 increase with increasing $\text{MnO}/(\text{MnO}+\text{CaF}_2)$ mass ratio. This tendency demonstrates that silicate networks are depolymerized as $\text{MnO}/(\text{MnO}+\text{CaF}_2)$ mass ratio increases. Notably, silicate networks are predominantly constituted by Q^3 and Q^2 , whereas Q^0 units are negligible. Therefore, silicate networks are mainly transformed from highly polymerized Q^3 to less polymerized Q^2 and Q^1 units as the $\text{MnO}/(\text{MnO}+\text{CaF}_2)$ mass ratio increases. The network-breaking role of MnO demonstrated in the present composition range can be explained as follows:

196 according to the analysis of McMillan,^[42] double-charged Mn^{2+} with larger ionization potential than
 197 Ca^{2+} may favor the higher charge concentration offered by the Q^2 ($=\text{Si}-2\text{O}^-$) sites. Moreover, Mn^{2+} ion
 198 is balanced with two adjacent corner-shared O^- ions due to its small $[\text{MnO}_6]$ cage.^[36, 42] Therefore,
 199 sheet-like silicate structures (Q^3) are mainly depolymerized into chain-like units (Q^2) by adding MnO ,
 200 as expressed in Equation [3].



202 The average non-bridging oxygen number per silicon atom (NBO/Si) value measures the degree
 203 of polymerization (DOP) of the melt, which can be calculated by Equation [4].^[9] Figure 4(d) shows
 204 NBO/Si values as a function of $\text{MnO}/(\text{MnO}+\text{CaF}_2)$ mass ratio. The NBO/Si value continuously
 205 increases from 1.29 to 1.72 with higher $\text{MnO}/(\text{CaF}_2+\text{MnO})$ mass ratio, indicating structural networks
 206 are depolymerized. The NBO/Si value constantly increases with increasing $\text{MnO}/(\text{MnO}+\text{CaF}_2)$ mass
 207 ratio because the added Mn-O bond incorporated the bridging oxygen (O^0) in Si-O-Si to form non-
 208 bridging oxygen (O^-), as described by Equation [5].



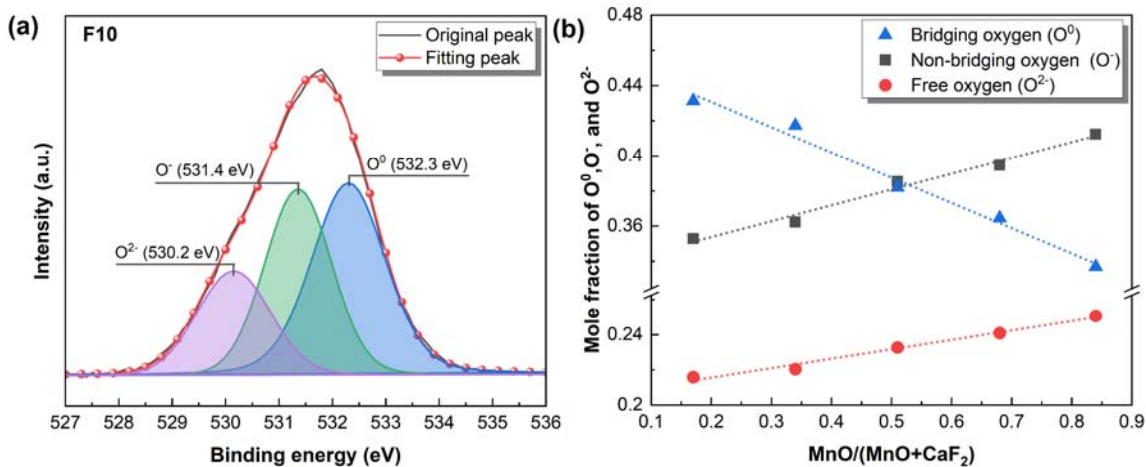


Figure 5—(a) Typical deconvolution results of O_{1s} for F10, and (b) mole fraction of different oxygen species as a function of MnO/(MnO+CaF₂) mass ratio.

Figure 5(a) presents a typical deconvoluted peak from O_{1s} XPS analysis for F10 (The rest devolution results are shown in Figure A2). O_{1s} XPS spectra were deconvoluted using the Gaussian method by assuming contributions from O⁰ (532.4 eV), O⁻ (531.5 eV), and O²⁻ (530.4 eV). Moreover, mole fractions of each oxygen species are obtained from the integrated areas of corresponding deconvoluted spectra. Mole fractions of different oxygen species are shown in Figure 5(b). It can be observed that the mole fraction of O⁰ significantly decreases, while that of O⁻ increases, with increasing MnO/(MnO+CaF₂) mass ratio. The equilibrium relationship of O⁰ and O⁻ in molten fluxes can be described as Equation [5].^[43] O²⁻ is supplied as a result of MnO dissociation due to its higher ionization energy. Hence, increasing MnO/(MnO+CaF₂) mass ratio may increase the concentration of O²⁻, driving Equation [5] to the direction towards depolymerization. As a result, a more depolymerized structure is induced by higher MnO/(MnO+CaF₂) mass ratio.

According to the above results, it can be summarized that flux viscosity decreases with higher MnO content due to the simplified network structure, although the details of structural roles of CaF₂

remain ambiguous. Thus, two hypotheses are proposed to reveal the structural roles of CaF_2 : (a) CaF_2 acts predominantly as a diluent and does not depolymerize network units; (b) the depolymerization ability of CaF_2 is weaker than that of MnO . These hypotheses can be further tested by investigating F_{1s} XPS and ^{19}F MAS-NMR spectra.

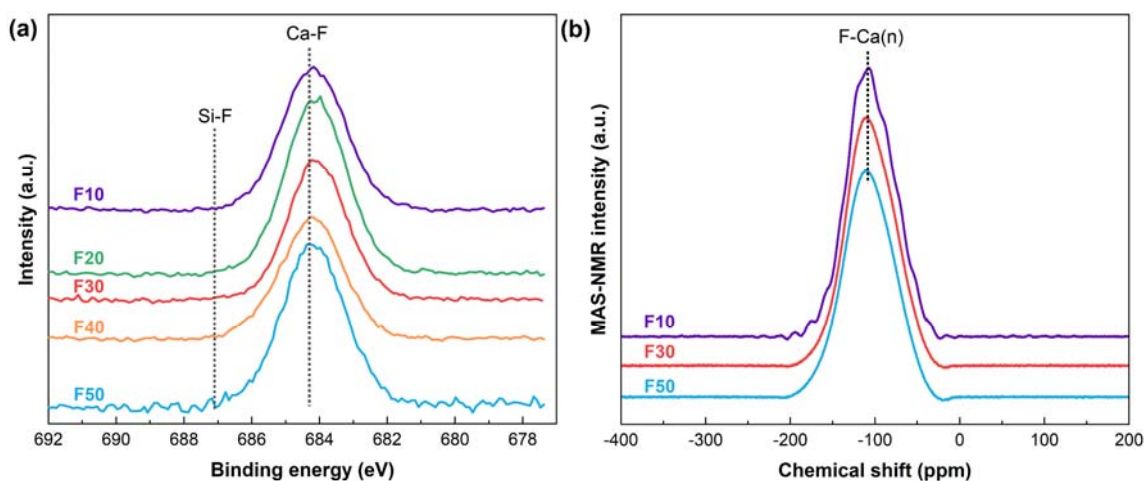


Figure 6—(a) F_{1s} XPS and (b) ^{19}F MAS-NMR spectra of the fluxes.

Figure 6(a) shows F_{1s} XPS spectra of the fluxes studied. Binding energies of pertinent referencing F-containing glasses, such as Ca-F bond (684.3 eV^[15,44]) and Si-F bond (687.1 eV^[44]), are marked in Figure 6(a). The spectra of all fluxes share similar symmetrical peaks yet with an unchanged center position (about 685.1 eV), which is close to that of the Ca-F bond rather than Si-F. Therefore, it can be seen that F^- is pre-dominantly coordinated with Ca^{2+} for the entire composition range of the targeted fluxes. Chemical shifts of ^{19}F MAS-NMR spectra can be used to measure the structural information of F in the fluxes.^[45] Typical ^{19}F MAS-NMR spectra of F10, F30, and F50 are shown in Figure 6(b). Three centers of the ^{19}F MAS-NMR spectra are located at -109.2 ppm, which can be assigned to F-Ca(n) species.^[45] F-Ca(n) species contain F^- in close proximity to Ca^{2+} and are charge-balanced by Ca^{2+} , which are not part of the silicate glass network.^[24] In addition, no distinct

peak of oxyfluoride species can be observed in ^{19}F NMR spectra, *i.e.*, $\text{Si}(\text{O})_x\text{F}_{4-x}$ at -123.4 to -134.5 ppm.^[45] Structural studies carried out by Kiczinski *et al.*^[46] showed that F^- preferentially bonds with cations carrying highest field strength ($\text{La}^{3+} > \text{Mg}^{2+} > \text{Ca}^{2+} > \text{Ba}^{2+} > \text{Na}^+$). F_{1s} XPS and ^{19}F MAS-NMR spectra results indicate that F^- predominantly bonds with Ca^{2+} rather than Si^{4+} , which proves the first hypothesis, *i. e.* CaF_2 acts predominantly as a diluent and does not depolymerize network units.

C. Relationship between Viscosity and Structure of the Flux

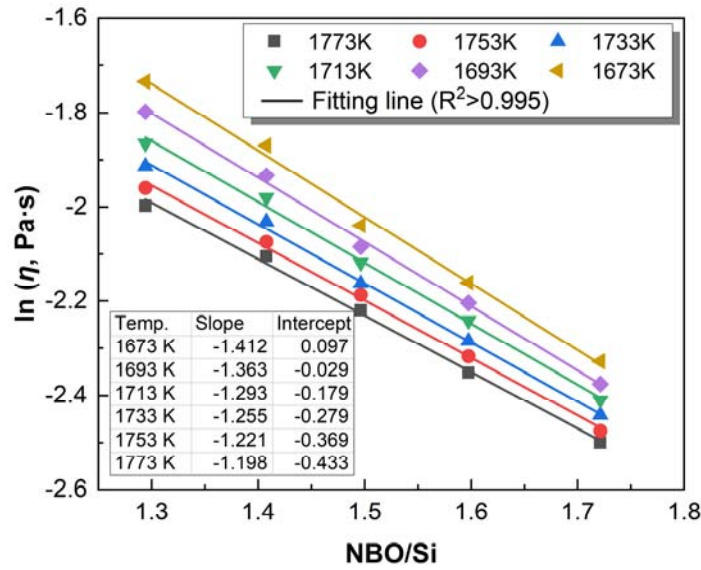


Figure 7—The relationship between logarithm viscosity and degree of polymerization of the fluxes.

The viscosity depends on DOP, which is ultimately dictated by the structure of the fluxes. The logarithm viscosity as a function of the NBO/Si is shown in Figure 7 in the temperature range of 1673 to 1773 K. It can be seen that the viscosity decreases linearly with increasing NBO/Si of the fluxes. In general, the logarithm viscosity and the NBO/Si can be described by the following Equation [6].

$$\ln \eta = a \times (\text{NBO/Si}) + b \quad [6]$$

where a and b are the slope and intercept of fitting lines, respectively. These fitting results further illustrate that NBO/Si can potentially be used as a DOP index to quantify the effect of silicate

structure on the viscosity of the flux.

IV. CONCLUSION

In this study, the effect of MnO substitution for CaF₂ on the viscosity and structure of molten CaF₂-SiO₂-MnO welding fluxes has been investigated and the relationship between viscosity and structure has been quantitatively identified. The main conclusions can be summarized as follows:

(1) With increasing MnO/(CaF₂+MnO) mass ratio in the CaF₂-SiO₂-MnO fluxes, viscosity and activation energy of the fluxes continuously decrease, and silicate networks in the fluxes mainly transform from highly polymerized Q^3 to depolymerized Q^2 and Q^1 units.

(2) F_{1s} XPS and ¹⁹F MAS-NMR spectra prove that F⁻ predominantly bonds with Ca²⁺ rather than Si⁴⁺, indicating CaF₂ acts as a diluent and does not effectively depolymerize the silicate network.

(3) The NBO/Si value increases with increasing MnO/(MnO+CaF₂) mass ratio and NBO/Si can potentially be used as a DOP index to quantify the influence of the silicate structure on flux viscosity.

ACKNOWLEDGMENTS

The authors sincerely acknowledge the financial support from the National Natural Science Foundation of China (Grant Nos., U20A20277, 52104295, 52150610494, 52011530180, and 52050410341), Research Fund for Central Universities (Grant Nos. N2125003, N2025025), and the Open Foundation of State Key Laboratory of Advanced Welding and Joining, Harbin Institute of Technology (Grant No. AWJ-22M23).

CONFLICT OF INTEREST STATEMENT

On behalf of all authors, the corresponding author states that there is no conflict of interest.

278 REFERENCES

- 279 1. J.B. Kim, J.K. Choi, I.W. Han, and I. Sohn: *J. Non-Cryst. Solids*, 2016, vol. 432, pp. 218-226.
- 280 2. V. Sengupta, D. Havrylov, and P.F. Mendez: *Weld. J.*, 2019, vol. 98, pp. 283s-313s.
- 281 3. S. Kumar and A. Shahi: *Mater. Design*, 2011, vol. 32, pp. 3617-3623.
- 282 4. C. Wang and J. Zhang: *Acta Metall. Sin.*, 2021, vol. 57, pp. 1126-1140.
- 283 5. V. Sengupta and P.F. Mendez: *Weld. J.*, 2017, vol. 96, pp. 334s-353s.
- 284 6. Y. Zhang, J. Zhang, H. Liu, Z. Wang, and C. Wang: *Metall. Mater. Trans. B*, 2022, vol. 53, pp. 1329-1334.
- 285 7. J. Zhang, T. Coetsee, H. Dong, and C. Wang: *Metall. Mater. Trans. B*, 2020, vol. 51, pp. 885-890.
- 286 8. J.B. Kim and I. Sohn: *ISIJ Int.*, 2014, vol. 54, pp. 657-663.
- 287 9. S. Seetharaman, A. McLean, R. Guthrie, and S. Sridhar: *Treatise on Process Metallurgy*, Elsevier Ltd., Oxford, 2014,
- 288 pp. 151-159.
- 289 10. Y. Zhang, T. Coetsee, H. Yang, T. Zhao, and C. Wang: *Metall. Mater. Trans. B*, 2020, vol. 51, pp. 1947-1952.
- 290 11. Z. Chang, K. Jiao, J. Zhang, X. Ning, and Z. Liu: *ISIJ Int.*, 2018, vol. 58, pp. 2173-2179.
- 291 12. T. Lienert, T. Siewert, S. Basu, and V. Acoff: *ASM Handbook, Volume 6A: Welding Fundamentals and Processes*,
- 292 ASM International Materials Park, OH, 2011, pp. 55-63.
- 293 13. Z. Pu, J. Huang, J. Li, H. Feng, X. Wang, and X. Yin: *J. Non-Cryst. Solids*, 2021, vol. 563, p. 120817.
- 294 14. G.H. Kim and I. Sohn: *J. Am. Ceram. Soc.*, 2019, vol. 102, pp. 6575-6590.
- 295 15. M. Hayashi, N. Nabeshima, H. Fukuyama, and K. Nagata: *ISIJ Int.*, 2002, vol. 42, pp. 352-358.
- 296 16. G.H. Zhang and K.C. Chou: *Ironmak. Steelmak.*, 2013, vol. 40, pp. 376-380.
- 297 17. Z. Wang, P. Tang, G. Wen, and Q. Liu: *ISIJ Int.*, 2019, vol. 59, pp. 367-374.
- 298 18. R. Xu, J. Zhang, X. Fan, W. Zheng, and Y. Zhao: *ISIJ Int.*, 2017, vol. 57, pp. 1887-1894.
- 299 19. J. Zhang, C. Wang, and T. Coetsee: *Metall. Mater. Trans. B*, 2021, vol. 52, pp. 1937-1944.
- 300 20. X. Yuan, M. Zhong, Y. Wu, and C. Wang: *Metall. Mater. Trans. B*, 2022, vol. 53, pp. 656-661.
- 301 21. J.H. Shim, Y.J. Oh, J.Y. Suh, Y.W. Cho, J.D. Shim, J.S. Byun, and D.N. Lee: *Acta Mater.*, 2001, vol. 49, pp. 2115-
- 302 2122.
- 303 22. Y. Kang, J. Jang, J.H. Park, and C. Lee: *Met. Mater. Int.*, 2014, vol. 20, pp. 119-127.
- 304 23. L. Zhang and S. Jahanshahi: *Metall. Mater. Trans. B*, 1998, vol. 29, pp. 177-186.
- 305 24. H. Kusumoto, R.G. Hill, N. Karpukhina, and R.V. Law: *J. Non-Cryst. Solids: X*, 2019, vol. 1, p. 100008.
- 306 25. H.S. Park, S.S. Park, and I. Sohn: *Metall. Mater. Trans. B*, 2011, vol. 42, pp. 692-699.
- 307 26. H. Ma, K. Jiao, J. Zhang, Y. Zong, J. Zhang, and S. Meng: *Ceram. Int.*, 2021, vol. 47, pp. 17445-17454.
- 308 27. M.S. Seo and I. Sohn: *J. Am. Ceram. Soc.*, 2019, vol. 102, pp. 6275-6283.
- 309 28. L. Zheng, H. Li, X. Wang, Z. Jiang, and H. Feng: *ISIJ Int.*, 2021, vol. 61, pp. 1784-1793.
- 310 29. J.B. Kim and I. Sohn: *ISIJ Int.*, 2014, vol. 54, pp. 2050-2058.
- 311 30. I. Sohn and D.J. Min: *Steel Res. Int.*, 2012, vol. 83, pp. 611-630.
- 312 31. G. Urbain, Y. Bottinga, and P. Richet: *Geochim. Cosmochim. Acta*, 1982, vol. 46, pp. 1061-1072.
- 313 32. Z. Yan, R.G. Reddy, X. Lv, Z. Pang, and C. Bai: *Metall. Mater. Trans. B*, 2018, vol. 50, pp. 251-261.
- 314 33. S. Lee and D.J. Min: *J. Am. Ceram. Soc.*, 2017, vol. 100, pp. 2543-2552.
- 315 34. J.S. Choi, T.J. Park, and D.J. Min: *J. Am. Ceram. Soc.*, 2021, vol. 104, pp. 140-156.
- 316 35. T.S. Kim, S.J. Jeong, and J.H. Park: *Met. Mater. Int.*, 2019, vol. 26, pp. 1872-1880.
- 317 36. J.H. Park: *ISIJ Int.*, 2012, vol. 52, pp. 1627-1636.
- 318 37. D. Virgo, B.O. Mysen, and I. Kushiro: *Science*, 1980, vol. 208, pp. 1371-1373.

319 38. S. Yu, S. Liu, M. Xie, Z. Li, and J. Wang: *Acta Metall. Sin.*, 1998, vol. 34, pp. 91-94.

320 39. Z. Wang, J. Zhang, M. Zhong, and C. Wang: *Metall. Mater. Trans. B*, 2022, vol. 53, pp. 1364-1370.

321 40. J.D. Frantza and B.O. Mysen: *Chem. Geol.*, 1995, vol. 121, pp. 155-176.

322 41. Y. Sun, H. Wang, and Z. Zhang: *Metall. Mater. Trans. B*, 2018, vol. 49, pp. 677-687.

323 42. P. McMillan: *Am. Mineral.*, 1984, vol. 69, pp. 645-659.

324 43. K.C. Mills: *ISIJ Int.*, 2016, vol. 56, pp. 1-13.

325 44. S. Hayakawa, A. Nakao, C. Ohtsutki, A. Osaka, S. Matsumoto, and Y. Miura: *J. Mater. Res.*, 1998, vol. 13, pp. 739-

326 743.

327 45. T.J. Kiczenski and J.F. Stebbins: *J. Non-Cryst. Solids*, 2002, vol. 306, pp. 160-168.

328 46. T.J. Kiczenski, L. Du, and J.F. Stebbins: *J. Non-Cryst. Solids*, 2004, vol. 337, pp. 142-149.

329

330

APPENDIX A: DECONVOLUTION RESULTS OF RAMAN AND XPS SPECTRA

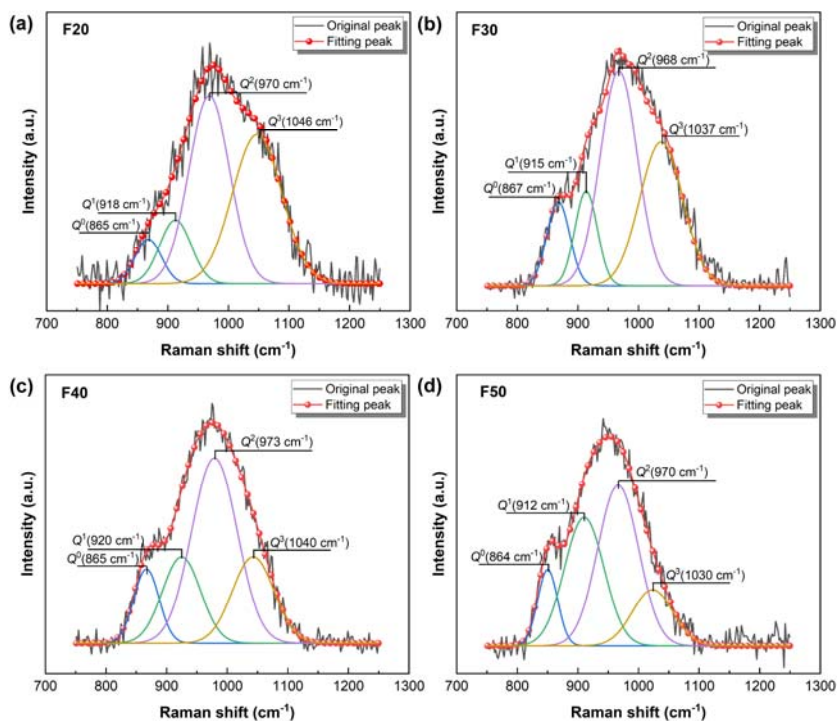


Figure A1—Fitting results of Raman spectra of (a) F20, (b) F30, (c) F40, and (d) F50.

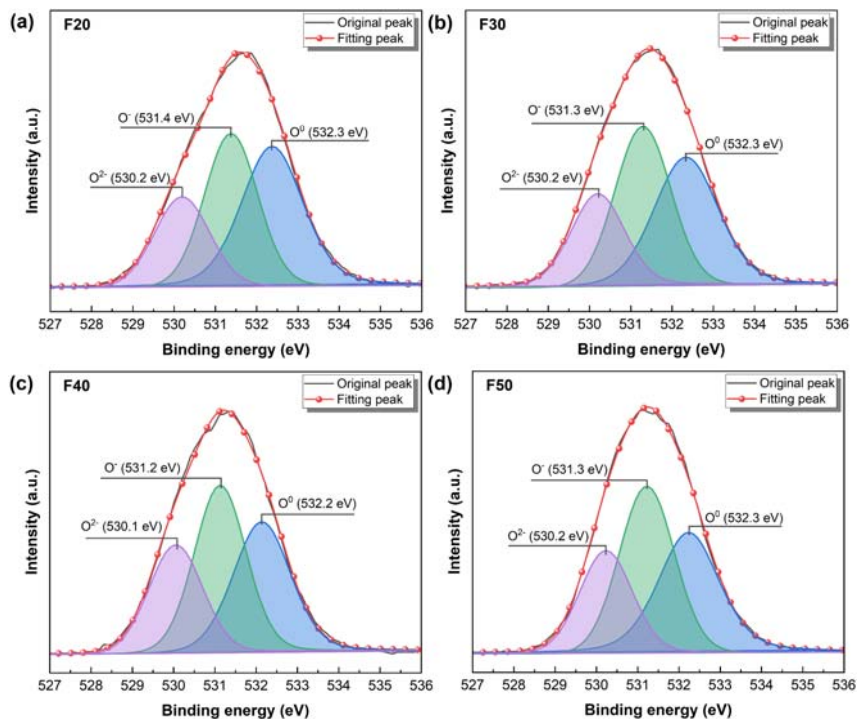


Figure A2—Fitting results of XPS spectra of (a) F20, (b) F30, (c) F40, and (d) F50.

LIST OF TABLE

Table I Chemical compositions of synthetic fluxes (mass pct).

LIST OF FIGURES

Figure 1—Flux viscosity as a function of (a) temperature, and (b) $\text{MnO}/(\text{MnO}+\text{CaF}_2)$ mass ratio.

Inset figure shows the viscosity range of flux with increasing $\text{MnO}/(\text{MnO}+\text{CaF}_2)$ mass ratio from 0.17 to 0.84 at given temperatures.

Figure 2—Arrhenius plot for the fluxes in fully liquid regions.

Figure 3—XRD patterns of the quenched fluxes.

Figure 4—(a) Raman spectra of the fluxes, (b) typical Raman deconvolution results of F10, (c) mole fraction of different $[\text{SiO}_4]$ -tetrahedra units as a function of $\text{MnO}/(\text{MnO}+\text{CaF}_2)$ mass ratio, and (d) degree of polymerization as a function of $\text{MnO}/(\text{MnO}+\text{CaF}_2)$ mass ratio.

Figure 5—(a) Typical deconvolution results of O_{1s} for F10, and (b) Mole fraction of different oxygen species as a function of $\text{MnO}/(\text{MnO}+\text{CaF}_2)$ mass ratio.

Figure 6—(a) F_{1s} XPS and (b) ^{19}F MAS-NMR spectra of the fluxes.

Figure 7—The relationship between logarithm viscosity and degree of polymerization of the fluxes.

Figure A1—Fitting results of Raman spectra of (a) F20, (b) F30, (c) F40, and (d) F50.

Figure A2—Fitting results of XPS spectra of (a) F20, (b) F30, (c) F40, and (d) F50.